

Pressurized organic electrodes enable practical and extreme batteries

Received: 19 April 2024

Accepted: 8 May 2025

Published online: 16 May 2025

Zhixiao Xu¹, Yunkai Xu², Yunkun Qiu³, Yan Cao³, Sergey Gasilov⁴, Ge Li⁵✉, Jun Lu²✉ & Xiaolei Wang¹✉

While organic batteries hold promise for sustainable energy storage, a considerable gap persists between research and application concerning testing conditions and cell cost. Here, we report pressurized organic electrodes tailored for practical applications. Outperforming prior organic electrodes, pressurized organic electrodes excel under challenging/extreme condition including high mass loadings (50–150 mg cm⁻²), active material fraction (up to 95%), low N/P ratio (0.8–2), and lean electrolyte, delivering high areal/volumetric capacity in full cells. Moreover, pressurized organic electrodes exhibit broad applicability, thriving in diverse battery systems (Li⁺/NH₄⁺/H⁺/Na⁺/Zn²⁺/Mg²⁺ ion batteries) and organic materials (molecule, polymer, salt), consistently demonstrating enhanced performance compared with unpressurized ones. The improved capacity, rate, and cycling performance of pressurized electrodes result from pressure-induced structural and property changes in organics including crystal orientation, enhanced π - π interaction, favorable electrode porosity/tortuosity, accelerated chemical reactivity, and boosted electronic conductivity. Along with simple, efficient, green, and cost-effective manufacturing features, pressurized organic electrodes offer a promising route towards organic battery application.

Organic batteries hold promise for sustainable development due to their natural abundance, tunable structures, low emissions, and potential cost-effectiveness^{1,2}. Over recent decades, numerous organics (comprising C, O, N, and S moieties) have been explored as battery electrode materials, spanning lithium, sodium, and zinc-ion batteries^{3–8}. Strategies have emerged to enhance battery performance via molecular design, polymer engineering, carbon hybridization, micro-/nanostructure construction, and electrolyte/separator modification^{8–14}. However, their practical applications still face grand challenges due to impractical testing conditions and elevated costs^{15,16}.

Organic materials of limited conductivity typically necessitate substantial quantities of conductive carbon, resulting in a lower fraction of active materials (AM, 30–70 wt.%) in electrodes, notably less than the 90–97 wt.% achieved with commercial inorganic

counterparts. Composed of light elements, organic materials inherently possess low density, and the density of resulting electrodes is even lower (e.g., 0.2 g cm⁻³) due to design of porous structure and presence of considerable carbon^{13,16}. This combined low density and AM fraction is usually accompanied with low mass loadings (typically 1–2 mg cm⁻²) in organic electrodes, compromising cell-level energy densities¹⁵. Ongoing efforts have sought to address these issues, yet yielding limited success^{5,13,17–21}. Moreover, most reported organic batteries are tested in half-cell or three-electrode configuration, lacking control over the N/P ratio and electrolyte quantity²², while some organic syntheses involve complex and costly catalyst-dependent processes²³. For organic batteries to become practically viable, they should satisfy the “three high, three low” (3H3L) condition: high mass loading, active material fraction, and electrode density, while

¹Department of Chemical and Materials Engineering, University of Alberta, Edmonton, AB, Canada. ²College of Chemical and Biological Engineering, Zhejiang University, Hangzhou, Zhejiang Province, China. ³Advanced Institute for Soft Matter Science and Technology (AISMST), South China University of Technology, Guangzhou, China. ⁴Canadian Light Source, Saskatoon, SK, Canada. ⁵Department of Mechanical Engineering, University of Alberta, Edmonton, AB, Canada.

✉ e-mail: ge.li@ualberta.ca; junzoelu@zju.edu.cn; xiaolei.wang@ualberta.ca

maintaining low cost, low N/P ratio, and minimal electrolyte usage in full-cell configurations¹⁵. Unfortunately, very few endeavors have simultaneously met demanding “3H3L” criteria^{15,24}. Solutions to break the current bottleneck remain an open challenge.

Inspired by pressure-enabled structural and performance modification in superconductors^{25–27}, optoelectronics^{28,29}, and cell stacks^{30–33}, we report the making of pressurized organic electrodes (POE) for practical batteries under “3H3L” condition. The pressure effects on the structure, property, and performance of organic materials/electrodes were systematically investigated. Under high pressure, a series of changes occur: morphological transformation, enhanced π - π interaction, narrowed band gap, oxygen vacancy formation, crystal orientation, porosity/tortuosity change as well as increased density, chemical reactivity, electronic conductivity, thermal stability, mechanical strength, and adhesive property. As a result, organic electrodes treated with higher pressure demonstrate better capacity, rate, and cycling performance in batteries. Under harsh condition of high-loading electrodes (51 mg cm⁻²), low N/P ratio (0.84), lean electrolyte (2.1 μ L mg⁻¹), a POE-based full cell demonstrates high areal capacity (6.6 mAh cm⁻²), fast charging capability (12 min) and a thousand cycle life with high initial Coulombic efficiency (CE) of 94.5% and stable CE of >99.95%. POE also enables extreme batteries working under high mass loadings of 150 mg cm⁻² (capacity: 22.5 mAh) and AM fraction of 95% (energy density: 112.6 Wh L⁻¹), far surpassing previous organic batteries. Moreover, POE technology could be broadly applied to different battery systems and organic materials, demonstrating one of the highest areal capacities (3–18 mAh cm⁻²) with leanest electrolyte among all reports. This establishes POE as a simple yet powerful technology for the practical implementation of organic electrodes.

Results

Making of POEs and pressure effects on organic structures

POE technology, detailed in Fig. 1a, comprises four steps: press, crush, mix, and press. Perylene-3,4,9,10-tetracarboxylic dianhydride (PTCDA) was used as a representative material due to its attributes of affordability and thermal stability. The application of POE in other organics will be discussed in the last section. Initially, pristine PTCDA powder is subjected to high pressure to form a self-supporting pellet, subsequently pulverized into fine particles, herein referred to as P-PTCDA. Following this, the P-PTCDA powder is mixed with carbon nanotubes (CNT) and subjected to a secondary pressurization step, giving rise to a free-standing, pressurized electrode. To investigate the effects of applied pressure on the structure, properties, and electrochemical performance of organic materials and electrodes, a series of compressive forces (0, 3, 6, 10 tons), corresponding to pressures of approximately 0, 232, 465, and 774 MPa, were applied. The resulting samples were designated as 0T-PTCDA (default as PTCDA), 3T-PTCDA, 6T-PTCDA, and 10T-PTCDA (default as P-PTCDA). Notably, compared to traditional slurry-based battery electrodes, our four-step POE technology offers a straightforward approach devoid of binders and collectors, boasting manufacturing speed (mere minutes), scalability (Supplementary Fig. 1), high yield (>98%, Supplementary Fig. 1), affordability, and environmental friendliness (free of solvents). Additionally, this method facilitates the fabrication of thick and dense electrodes, exemplified by electrodes of hundreds of milligrams in mass and millimeters in thickness (Fig. 1a and Supplementary Fig. 2).

The impact of pressure on the structural characteristics of the PTCDA molecule was initially investigated via electron microscopy and spectroscopy techniques. Scanning electron microscopy (SEM) and transmission electron microscopy (TEM) unveiled a transformative effect: the one-dimensional PTCDA nanorods (Fig. 1b) underwent a collapse and fusion process, resulting in the formation of two-dimensional P-PTCDA nanosheets with significantly enlarged dimensions (Fig. 1c, and Supplementary Fig. 3). Spectroscopic analyses, including Fourier transform infrared (FTIR) spectra and ultraviolet-

visible (UV-vis) spectra, illuminated notable peak shifts in P-PTCDA compared to its pristine counterpart, indicative of stronger intermolecular π - π interactions within P-PTCDA (Supplementary Figs. 4–5 and Supplementary Note 1). Consequently, P-PTCDA exhibited a narrower optical band gap relative to PTCDA (1.80 vs. 2.05 eV, Fig. 1d). Further insights were gained from X-ray photoelectron spectroscopy (XPS) results, with full spectra revealing a reduction in oxygen content in P-PTCDA, implying oxygen loss consequent to pressure treatment (Supplementary Fig. 6 and Supplementary Note 2). High-resolution XPS C 1s and O 1s spectra evidenced diminished C-O-C peaks at 286.7 eV and 533.4 eV in P-PTCDA compared to PTCDA, indicating oxygen loss specifically at the C-O-C site. This oxygen vacancy led to a notable negative shift in the C=O peak from 531.6 eV in PTCDA to 531.4 eV in P-PTCDA, suggesting a more negative charge density at the C=O site in P-PTCDA, potentially favorable for rapid coordination reactions with ions in battery applications. The presence of oxygen vacancy was further corroborated by electron paramagnetic spectroscopy, which revealed more signals of unpaired electrons in P-PTCDA relative to PTCDA (Fig. 1e). Notably, given the very high conversion rate from PTCDA to P-PTCDA (>99%), it is inferred that oxygen vacancy is predominantly introduced at the nanoscale surface of P-PTCDA, which was verified by depth-profile XPS (Supplementary Fig. 7).

The influence of pressure on the crystalline structure of PTCDA was explored using various X-ray diffraction (XRD) techniques. Powder XRD patterns (Fig. 1f) identified a mixed phase composition dominated with the β -phase in PTCDA powder¹⁸, with detailed crystal structures provided in Supplementary Fig. 8. Pelletization of PTCDA led to notable changes: while the majority of peaks were unchanged, two peaks at 27.6° and 28° converged into a single broader peak at 27.7°. This alteration was maintained after crushing, as shown by similar patterns between P-PTCDA powder and PTCDA pellets (Supplementary Fig. 9). Overlaying the XRD patterns of PTCDA and P-PTCDA (Fig. 1g) highlighted that post-compression, P-PTCDA exhibited broader peaks with an increased full width at half maximum, indicating a reduction in crystallite size and the introduction of defects, probably due to oxygen vacancy formation. Despite these broader peaks, the pattern of P-PTCDA largely corresponded to those of β -PTCDA, indicating negligible phase transformation. However, a noticeable shift in peaks towards higher angles suggested a decrease in crystal plane distances, attributed to enhanced π - π interactions resulting from the applied pressure. As the pressure incrementally rose from low (3 tons) to medium (6 tons) and then to high (10 tons), the intensity ratio of the 27.6° peak to the 12.5° peak increased from 1.07 to 1.15, and finally to 1.32, highlighting a progressive enhancement in π - π interactions with increasing pressure (Supplementary Fig. 10). Two-dimensional wide-angle X-ray diffraction (WAXD) ring patterns from PTCDA pellets confirmed the dominance of the β -PTCDA phase alongside traces of α -PTCDA, with reflections corresponding to the 020, 021, 012, 022, 041, 032, 042, and 052/102 planes, indexed according to the unit cell parameters (Fig. 1h). Geometric analyses of the reciprocal lattices revealed the alignment of P-PTCDA molecules along the b-axis within the β -phase unit cell at an angle of 38°. Crucially, the b-axis orientation perpendicular to the pellet surface enabled well-organized π - π stacking parallel to the substrate (Fig. 1i). This structural alignment facilitates the formation of ordered open channels, which may potentially facilitate rapid ion and electron transport during battery cycling. By contrast, the 2D WAXD ring pattern from PTCDA powder displayed a lack of distinctive features, indicating a random molecular orientation (Fig. 1j).

The preceding observations elucidate the pressure-induced structural transformations within PTCDA at the material level. To comprehensively assess alterations in PTCDA and P-PTCDA electrodes, microscopy and tomography techniques were employed. SEM images unveiled distinct characteristics in the two electrodes, with felt-like sheets of woven CNT encapsulating organic materials and exhibiting

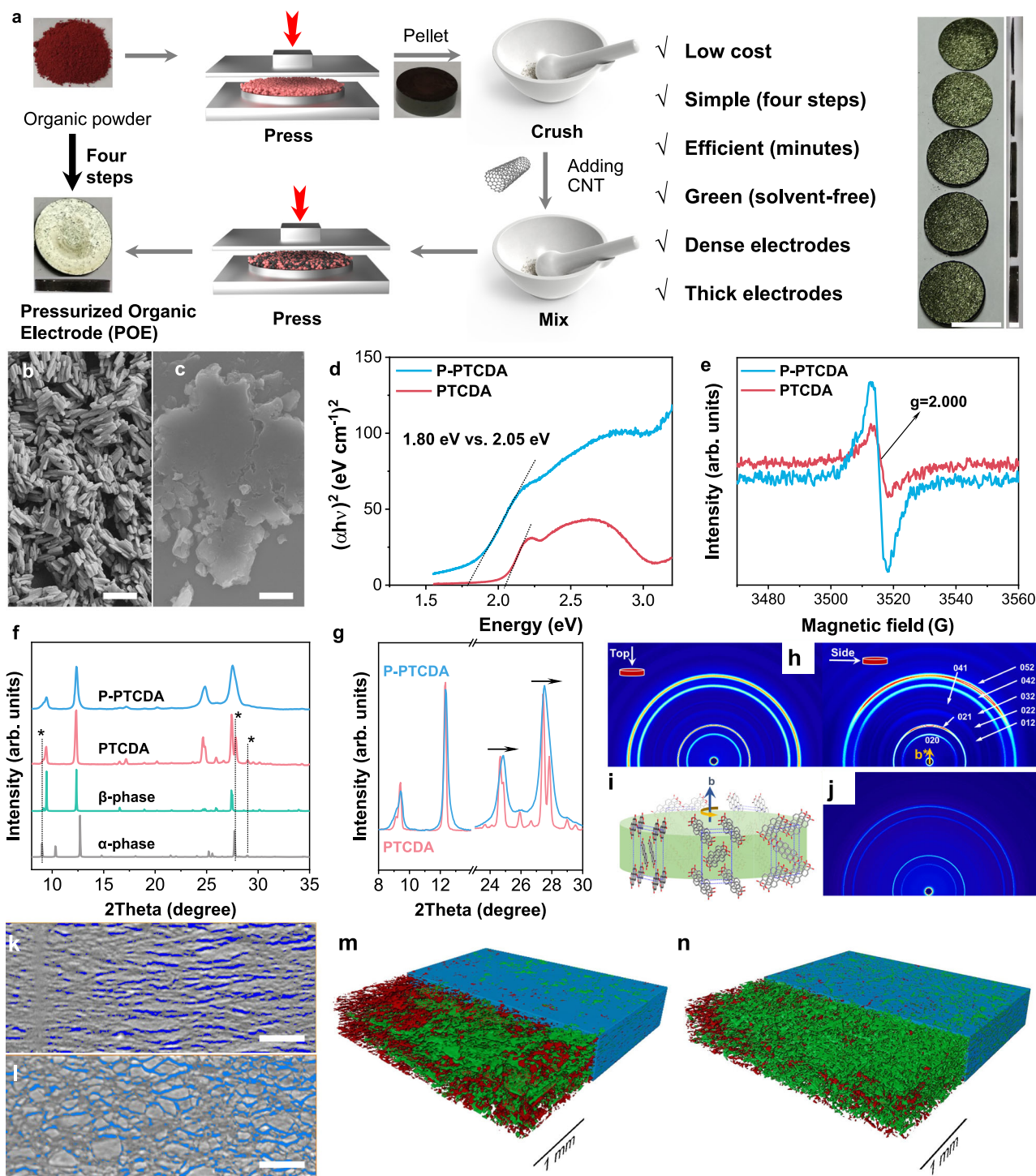


Fig. 1 | Preparation of POEs and structural characterization. **a** Schematic illustration for POE preparation. Inset shows the digital photos of pristine PTCDA powder, PTCDA pellet, and POEs. Scale bar: left 1 cm, right, 2 mm. Pressure effects on the structure of PTCDA and its electrode: SEM images of **b** PTCDA and **c** P-PTCDA. Scale bars, 2 μm . **d** Tauc plot derived from UV-vis spectra, and **e** EPR spectra of PTCDA and P-PTCDA. **f, g** XRD patterns of PTCDA and P-PTCDA along with calculated α - and β -phase PTCDA. 2D WAXD patterns of **h** PTCDA pellet (left:

top scan, right: side scan, as shown in insets) and **j** PTCDA powder. **(i)** Schematic illustration of crystal orientation in the POE electrode. Synchrotron-based X-ray computed tomography images of **k** PTCDA and **l** P-PTCDA electrode (blue color: porous structure) and corresponding reconstructed and rendered images of **m** PTCDA and **n** P-PTCDA electrode. Scale bars, 200 μm . Green, red, and blue color represents interconnected pores, isolated pores, and molecule-CNT composites, respectively. Source data are provided as a Source Data file.

differing porous structures (Supplementary Figs. 11–12). Synchrotron-based X-ray computed tomography further revealed that while the PTCDA electrode exhibited porous channels parallel to the electrode surface (Fig. 1k), the P-PTCDA electrode showcased porous channels oriented towards the electrode surface (Fig. 1l). This orientation

disparity resulted in decreased tortuosity in the P-PTCDA electrode (2.3 vs. 4.5 in PTCDA). Moreover, the P-PTCDA electrode exhibited a higher proportion of interconnected pores (86.4% vs. 68.9%) and fewer isolated pores compared to the PTCDA electrode (Fig. 1m, n, Supplementary Figs. 13–14). The orientation of porous channels and the

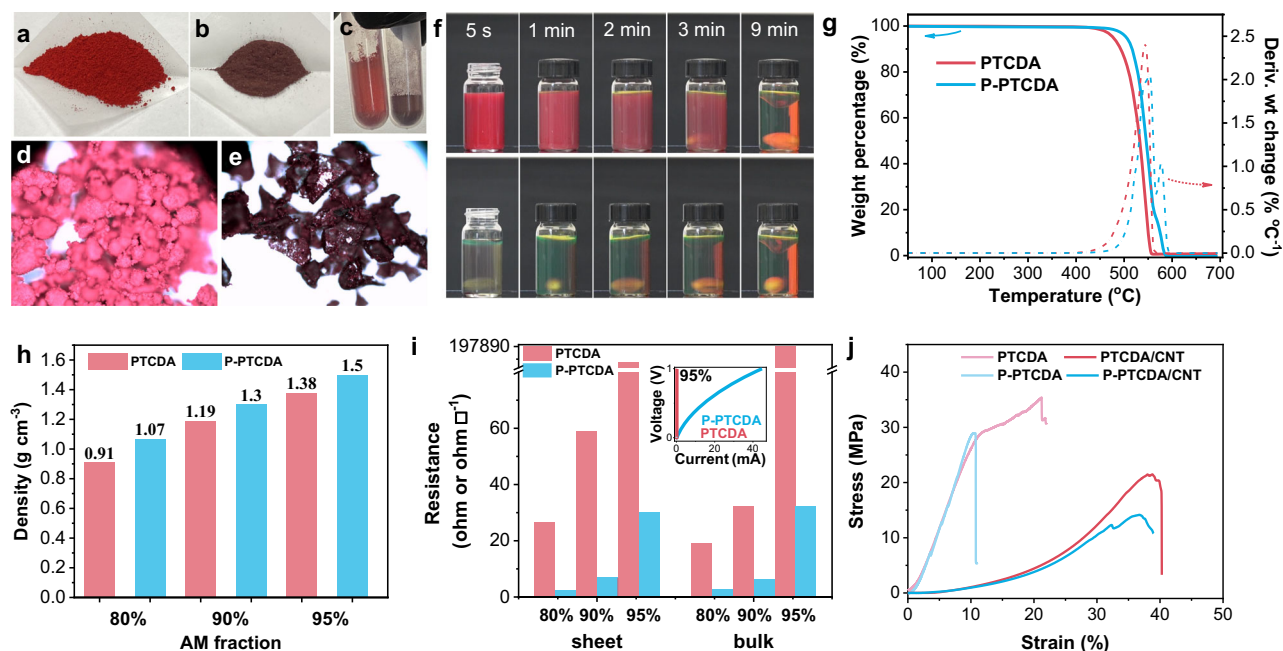


Fig. 2 | Pressure effects on properties of organic materials and electrodes.

Digital photos of PTCDA (a) and P-PTCDA powder (b) of equal mass, along with their natural state in a plastic tube (c). Optical microscope images of d PTCDA, and e P-PTCDA. f Digital photos showing the chemical reaction between lithium hydroxide and PTCDA (above images) or P-PTCDA (below images) at different time.

g TGA and DTA curves of PTCDA and P-PTCDA. h Density, i sheet and bulk resistance of PTCDA and P-PTCDA electrodes with different AM fractions. j Stress-strain curves of PTCDA and P-PTCDA-based pellets under compression. Source data are provided as a Source Data file.

abundance of interconnected pores in the P-PTCDA electrode may render it conducive to electrolyte/ion transport during battery cycling (Supplementary Movie 1–2). Confocal microscope images reveal that P-PTCDA electrode has smoother surface with lower roughness value than that of PTCDA electrode (Supplementary Fig. 15). These multifaceted characterizations underscore the pivotal role of pressure in sculpting the structural attributes of PTCDA materials and electrodes, potentially enhancing their electrochemical performance and applicability in energy storage technologies.

Pressure effects on properties of organic material and electrode

The pressure-induced structural alterations in PTCDA correspondingly engender significant property modifications in P-PTCDA. A notable transformation is the powder color, changing from bright red in PTCDA (Fig. 2a, d) to a darker hue in P-PTCDA (Fig. 2b, e), indicative of an irreversible piezochromic response (Supplementary Fig. 16)³⁴. This color shift correlates with a red shift observed in UV-vis spectra³⁵. Additionally, a marked increase in powder density is observed in P-PTCDA compared to PTCDA under natural conditions (Fig. 2a–c). Chemical reactivity assessments reveal distinctive behavior between PTCDA and P-PTCDA. Upon reaction with lithium hydroxide, P-PTCDA demonstrates rapid color change within 5 s and complete hydrolysis in a shorter duration than PTCDA, indicating faster reaction kinetics (Fig. 2f, Supplementary Fig. 17 and Movie 3). This accelerated reactivity is attributed to electron delocalization and oxygen vacancy at the C–O–C site in P-PTCDA, rendering it susceptible to hydroxide anion attack¹⁷. Conversely, both PTCDA and P-PTCDA exhibit stability in acidic and neutral solutions (Supplementary Fig. 18). Thermal gravimetric analysis reveals the superior thermal stability of P-PTCDA, with a 50 °C increase in decomposition temperature compared to PTCDA in air (Fig. 2g), attributed to the presence of oxygen vacancy mitigating oxidation reaction. Moreover, density evaluations of PTCDA and P-PTCDA electrodes, varying in AM and CNT fractions, demonstrate that P-PTCDA electrodes exhibit higher densities than their PTCDA counterparts at equivalent AM fractions (Fig. 2h). Electrical

conductivity assessments reveal decreased sheet and bulk resistance with increasing CNT content, with P-PTCDA electrodes displaying lower resistance than PTCDA electrodes at same AM fractions (Fig. 2i). Notably, at a high AM fraction of 95%, P-PTCDA electrodes demonstrate a three-orders-of-magnitude improvement in conductivity compared to PTCDA electrodes, attributed to crystal orientation, enhanced π – π interaction, and oxygen vacancy in P-PTCDA. Mechanical property assessments reveal the brittleness of PTCDA and P-PTCDA pellets, contrasting with the ductility observed in PTCDA/CNT and P-PTCDA/CNT pellets (Fig. 2j and Supplementary Movie 4). The latter exhibit notable reversible strains of up to 38% and 32.3%, respectively. Similar mechanical behavior was observed when testing pellets in the presence of electrolyte (Supplementary Figs. 19–20), suggesting the ductility enabled by CNT could buffer volumetric changes during battery operation^{36–38}. Of note, P-PTCDA and P-PTCDA/CNT pellets exhibit slightly weaker compression strength and strain compared to their PTCDA counterparts, likely due to less exposed surface area of aggregated P-PTCDA particles with less inter-particle interactions. This was further substantiated by the weaker adhesive property of P-PTCDA relative to PTCDA (Supplementary Fig. 21 and Supplementary Note 3), which manifests in less material loss during electrode preparation. Free-fall experiments validate the robust mechanical integrity of both PTCDA and P-PTCDA electrodes under varying pressure treatments or differing AM fractions, affirming their overall robust mechanical properties (Supplementary Movie 5). Overall, with enhanced chemical reactivity, thermal stability, electrical conductivity, and mechanical properties, POEs hold promise for electrochemical applications.

Pressure effects on practical lithium battery performance

The pressure effect on battery performance of POEs was assessed in aqueous lithium-ion batteries with PTCDA or P-PTCDA as the negative electrode, LiMn_2O_4 as the positive electrode, and 4 mol per liter lithium triflate in water (4 M LiOTf) as the electrolyte. Full cells were tested under “3H3L” condition including high-loading electrodes (P-

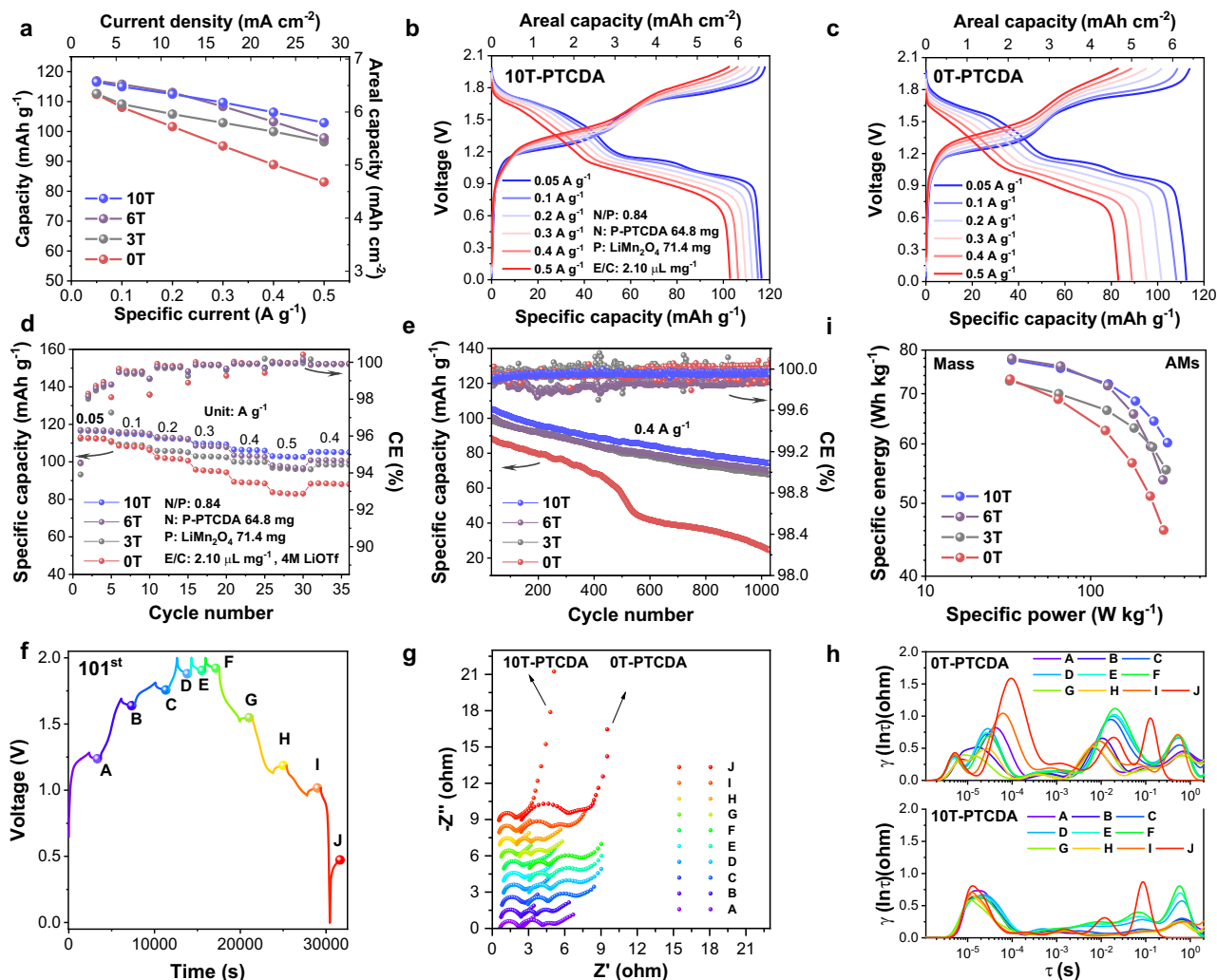


Fig. 3 | Pressure effects on battery performance. **a** capacity-rate profiles of POEs treated with different pressure. Voltage-capacity profiles of **b** 10T-PTCDA and **c** 0T-PTCDA cell at rates of 0.05–0.5 A g⁻¹. **d** Rate and **e** cycling performance of 0T-, 3T-, 6T-, and 10T-PTCDA cells. **f** Charge-discharge profile, resting period, and different

collected points for the in situ EIS spectra, **g** EIS spectra of 0T- and 10T-PTCDA cells at the 101st cycle collected at different points. And corresponding **h** DRT profiles. **i** Comparison of specific energy between 0T-, 3T-, 6T-, and 10T-PTCDA cells. Source data are provided as a Source Data file.

PTCDA: 64.8 mg, LiMn₂O₄: 71.4 mg, area: 1.267 cm², low N/P ratio (0.84), and lean electrolyte (E/C = 2.1 μL mg⁻¹, defined as the ratio of electrolyte to positive electrode). Due to the free-standing feature, electrodes could be assembled into the cell without the need of extra binder and current collector (Supplementary Fig. 22 and Supplementary Movie 6). This feature significantly reduces the fraction of inactive materials and increase energy/power density at the cell level^{5,19}. For comparison, 0T-PTCDA, 3T-PTCDA, 6T-PTCDA, and 10T-PTCDA were tested under the same condition.

The rate performance of four cells is compared in Fig. 3a, d. At current densities ranging from 0.05 to 0.5 A g⁻¹, 10T-PTCDA cell delivers higher specific capacities (116.5–102.9 mAh g⁻¹) than its 6T-, 3T-, and 0T-PTCDA counterparts. All four cells exhibit high initial Coulombic efficiencies (ICE), with the 10T-PTCDA achieving the highest value of 94.6% (Supplementary Fig. 23). Galvanostatic charge/discharge curves of 10T-PTCDA and 0T-PTCDA at different rates are shown in Fig. 3b, c, respectively. At a low rate of 0.05 A g⁻¹, both cells display five discharge plateaus at 1.69, 1.55, 1.44, 1.13, and 0.97 V. However, at higher rates, only three voltage plateaus remain—at 1.60, 1.34, and 1.00 V—highlighting a multi-step storage mechanism (Supplementary Fig. 24). Similar voltage plateaus are observed in 3T- and 6T-PTCDA cells (Supplementary Fig. 25a, b). Notably, thick 10T-PTCDA

electrode enables high areal capacities ranging from 5.80 to 6.56 mAh cm⁻² at rates of 2.82–28.2 mA cm⁻², surpassing the 0T-, 3T-, and 6T-PTCDA electrodes. Cycling performance at a high rate of 0.4 A g⁻¹ (15 min duration) is shown in Fig. 3e. While 0T-PTCDA cell shows rapid capacity decay—retaining only 60% after 513 cycles—POEs demonstrate substantially improved stability. The 10T-, 6T-, and 3T-PTCDA cells retain 70.7%, 69.5%, and 68.8% of their initial capacities after 1000 cycles, and maintain 60% capacity through 1690, 1587, and 1460 cycles, respectively (Supplementary Fig. 25c). In addition to its higher ICE, the 10T-PTCDA cell also exhibits superior CE values during cycling, remaining stable between 99.95 and 99.99% over 2000 cycles, in contrast to the fluctuating CE observed in the 0T-, 3T-, and 6T-PTCDA cells.

In situ electrochemical impedance spectroscopy (EIS) tests were conducted to elucidate the dynamics of charge transfer and internal resistance throughout cycling (Fig. 3f and Supplementary Figs. 26–27). Initially, the 0T-PTCDA cell exhibits slightly lower resistance during the first two cycles; however, its resistance significantly exceeds that of the 10T-PTCDA cell after 100 cycles (Fig. 3g). As the cycling progresses from the 1st to the 2nd and then to the 101st cycle, the 0T-PTCDA cell demonstrates a progressive increase in contact resistance, initially decreasing and then increasing charge-transfer resistance, and an

unstable interface as indicated by additional semi-cycles at the 101st cycle, likely due to side products from active material dissolution. By contrast, the 10T-PTCDA cell exhibits a continuous decrease in contact and charge-transfer resistance, alongside a stable interface, even after 100 cycles, which can be attributed to enhanced π - π interaction inhibiting material dissolution and side reactions. The superiority of 10T-PTCDA cell over 0T-PTCDA cell was confirmed by the distribution of relaxation times (DRT) profiles, which demonstrated much lower and more stable resistance at different timescale when comparing 10 T cell with 0 T cell (Fig. 3h)³⁹.

Specific energy and power of four cells (0T-, 3T-, 6T-, 10T-PTCDA) were calculated based on AM (Fig. 3i). 10T-PTCDA cell achieved the specific energy of 77.6 Wh kg⁻¹ (at 33.3 W kg⁻¹), higher than other three cells (~73 Wh kg⁻¹). 10T-PTCDA cell also delivered the highest areal/volumetric energy densities (8.35 mWh cm⁻²/86.4 Wh L⁻¹) and power densities (31.5 mW cm⁻²/326 W L⁻¹) among them (Supplementary Fig. 28). These results suggest higher pressure is beneficial to the reversibility, capacity, rate, and cycling performance of batteries due to pressure-boosted chemical reactivity and enhanced electrical conductivity as well as stronger π - π interaction with less organic dissolution.

POE-based batteries working under extreme condition

Encouraged by the remarkable performance of POEs, we conducted further tests on 10T-PTCDA electrodes under extreme conditions, including high mass loadings and AM fractions. Increasing the mass loading from 50 to 100 and 150 mg cm⁻² resulted in a proportional increase in electrode thickness, from 0.55 to 1.05 and 1.61 mm, respectively. As depicted in Fig. 4a–d, based on these thick electrodes, the areal capacity linearly increased from 6.6 to 11.5 and 17.8 mAh cm⁻², while preserving discharge voltage plateaus (Fig. 4e, f). Notably, under low N/P ratio and lean electrolyte conditions, the 100 mg cm⁻² and 150 mg cm⁻² cells could stably operate for 200 cycles (65.7% retention) and 30 cycles (90.3% retention) with high ICE of 94.14 and 95.18%, stable CE of 97–99.5%, and accumulated capacities of 2060 and 642 mAh, respectively (Fig. 4g and Supplementary Figs. 29–31).

Conversely, as the AM fraction increased from 80 to 90% and 95% while maintaining a high loading of ~50 mg cm⁻², the density of corresponding electrodes increased from 1.07 to 1.3 and 1.5 g cm⁻³. Figure 4h illustrates that cells based on high-AM fraction electrodes (90–95%) exhibited almost the same specific capacity values as those with lower AM fractions (80%) at 0.05–0.3 Ag⁻¹. Furthermore, POEs of 90% and 95% AM fractions enabled fast charging capability (fully charged in 15 min) and good cycling stability even under extreme condition. After 500 cycles, the 90% AM fraction retained 70% of its initial capacity, while the 95% AM fraction retained 60%, as depicted in Fig. 4i and Supplementary Figs. 32–35. Under these extreme conditions, the utilization ratio of these thick and dense POEs remains as high as 88.2–94.0% (Supplementary Fig. 36). The achievement of 150 mg cm⁻² loading, 95% AM fraction, 17.8 mAh cm⁻² areal capacity, and high utilization in our work far surpasses previously reported organic electrodes^{2–5,10,14,22,23,40–43}, such as polypeptides, quinones, anhydrides, salts, and conducting polymers (Fig. 4j, Supplementary Table 1), and even outperforms most inorganic electrodes^{12,44–48}.

With these impressive results, we further calculated energy/power densities (based on electrodes) and analyzed the overall cost of these cells to evaluate their application potentials. The combination of 95% AM and 50 mg cm⁻² demonstrates the highest energy density of 112.6 Wh L⁻¹ and specific energy of 70.3 Wh kg⁻¹, while the highest areal energy density of 21.5 mWh cm⁻² is achieved in the 80% AM-150 mg cm⁻² cell (Fig. 4k and Supplementary Fig. 37). Additionally, the 95% AM-50 mg cm⁻² cell demonstrates remarkable cost-effectiveness, with electrode and cell materials costing as low as \$56.8 kWh⁻¹ and \$167.7 kWh⁻¹, respectively (Fig. 4k, Supplementary Fig. 38, Supplementary Note 4, and Supplementary Table 2). These costs are

competitive with those of established commercial lithium-ion batteries and aqueous batteries, highlighting the substantial promise of this POE technology for imminent commercialization.

POEs for various battery systems

In addition to lithium-ion batteries, the POE technology proves to be versatile and applicable to other battery systems, including ammonium and zinc ion batteries. Despite previous reports considering β -PTCDA unsuitable for aqueous ammonium and zinc ion batteries^{19,34,49}, the application of POE technology unveils its high performance for NH₄⁺ and Zn²⁺ ion storage. In the ammonium ion battery system, thick P-PTCDA-based full cells exhibit large areal capacities (2.38–2.73 mAh cm⁻² at 4.64–18.6 mA cm⁻²) and high voltage of -1.25 V (Fig. 5a, b), outperforming previously reported values (Supplementary Table 3). Similarly, when employed as a positive electrode for Zn²⁺ ion storage, P-PTCDA demonstrates fast and stable cycling even at high loadings (26.7–40.7 mg cm⁻²), delivering large areal capacities that surpass those of PTCDA electrodes (Fig. 5c, d, and Supplementary Fig. 39) and rank among the best in zinc-organic batteries (Supplementary Table 4). Additionally, POE technology serves as an outstanding platform for assessing the efficacy of electrolytes and the reversibility of metal electrodes under high areal capacities in a full-cell configuration (Supplementary Figs. 40–42 and Supplementary Note 5). Given the low redox potential of P-PTCDA (-0.5 V vs. Zn²⁺/Zn) which is slightly above the hydrogen evolution reaction potential (theoretical) in aqueous electrolytes, P-PTCDA electrodes are more suitable as negative electrodes for aqueous battery systems.

Furthermore, POE technology finds widespread application in proton, sodium, and magnesium ion batteries (Fig. 5e). Proton batteries utilizing P-PTCDA as the negative electrode achieve significant performance enhancements, including one of the largest areal capacity (3.17 mAh cm⁻²), highest rate (28.7 mA cm⁻²), extended cycle life (800 cycles), and high CE values (>99%) compared to their unpressurized counterparts (Fig. 5f and Supplementary Fig. 43). Similarly, in sodium batteries, P-PTCDA enables a long life with high capacity retention (100% after 1000 cycles, 2 mAh), representing one of the most stable aqueous sodium ion batteries (Fig. 5f and Supplementary Figs. 44–45). Moreover, P-PTCDA demonstrates promising performance in magnesium ion batteries, achieving large areal capacities up to 4 mAh cm⁻² and respectable cycle life (Supplementary Fig. 46). These achievements in ammonium, zinc, proton, sodium, and magnesium batteries underscore the versatility and effectiveness of POE technology across various battery systems, positioning it as a promising technology for practical batteries.

POEs for different organic materials

The feasibility and efficacy of the proposed POE technology were investigated beyond PTCDA, including nitrogen-containing 3,4,9,10-perylenetetracarboxylic diimide (PTCDI), flexible chain-bridged polyimide (PI), and zinc thiolate (ZnSN) as research subjects (Fig. 6a). Termed P-PTCDI, P-PI, and P-ZnSN respectively, their pressurized counterparts exhibited apparent morphological transformations after pressure treatment (Fig. 6b–d and Supplementary Fig. 47). While pristine PTCDI, PI, and ZnSN showcased nanofiber, microflower, and urchin-shaped morphologies, pressurized variants presented as aggregated bulky structures assembled by two-dimensional sheets. Observable color changes after pressure treatment (Supplementary Fig. 48 and Supplementary Note 6) hinted at alterations in electronic structure, confirmed by peak shifts in UV-Vis spectra and narrowed band gaps (Fig. 6e and Supplementary Fig. 49). Additionally, FTIR spectra and XRD patterns revealed enhanced π - π interactions and reduced crystal size in pressurized samples compared to pristine ones (Supplementary Fig. 50). Pressure densification was evident at both the material and electrode level, as reflected in reduced occupied space at the same mass and higher density attained in POEs (Fig. 6f).

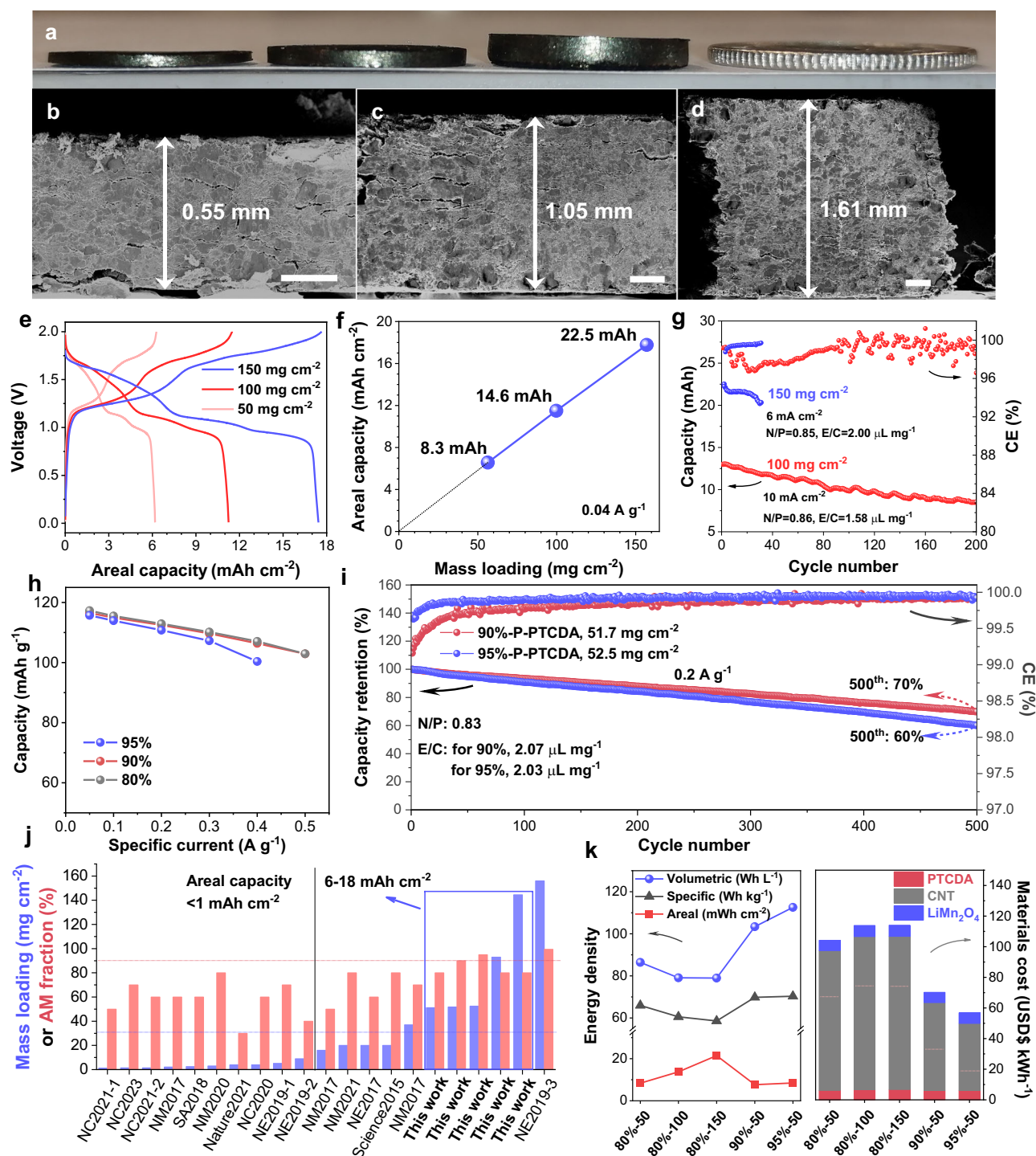


Fig. 4 | POE-based batteries working under high mass loadings and AM fraction.

a Digital photos of POEs with millimeter thickness (and a Canadian dime with 1.20 mm thickness) and their corresponding (b–d) cross-section SEM images: **b** -50 mg cm⁻², **c** -100 mg cm⁻², **d** -150 mg cm⁻². Scale bars, 200 μm. **e** Charge-discharge profiles of thick POEs with different mass loadings. **f** Plot of areal capacity against mass loading. **g** Cycling performance of thick POEs (mass loadings: -100 mg cm⁻² and -150 mg cm⁻²) under low N/P ratio and lean electrolyte.

h Capacity-rate profiles of batteries based on POEs with different AM fraction (80%, 90%, and 95%). **i** Capacity retention and CE values of 90%-, and 95%-P-PTCDA cells during long cycling. **j** Comparison of POEs with reported battery electrodes in terms of mass loadings, AM fraction, and areal capacity. **k** Gravimetric/areal/volumetric energy density and cost analysis of cells based on different POEs. Source data are provided as a Source Data file.

Comparative evaluations against unpressurized electrodes demonstrated lower sheet and bulk resistance in all organics within POEs (Fig. 6g). Mechanical robustness of these POEs was confirmed by free-fall experiments (Supplementary Movie 7).

Battery performance assessments were conducted on PTCDA, P-PTCDA, PI, and P-PI electrodes in lithium-ion batteries, and on ZnSN and

P-ZnSN electrodes in zinc batteries under “3H3L” conditions. Notably, P-PTCDA cells exhibit higher areal capacities (4–6 mAh cm⁻²), faster charging rate (2.85–22.8 mA cm⁻²), and longer cycling life (63% retention after 1000 cycles), surpassing PTCDA cells in all metrics (Fig. 6h, k and Supplementary Fig. 51). Similarly, P-PI cells demonstrate superior capacity retention and performance compared to PI cells (Fig. 6i, l and

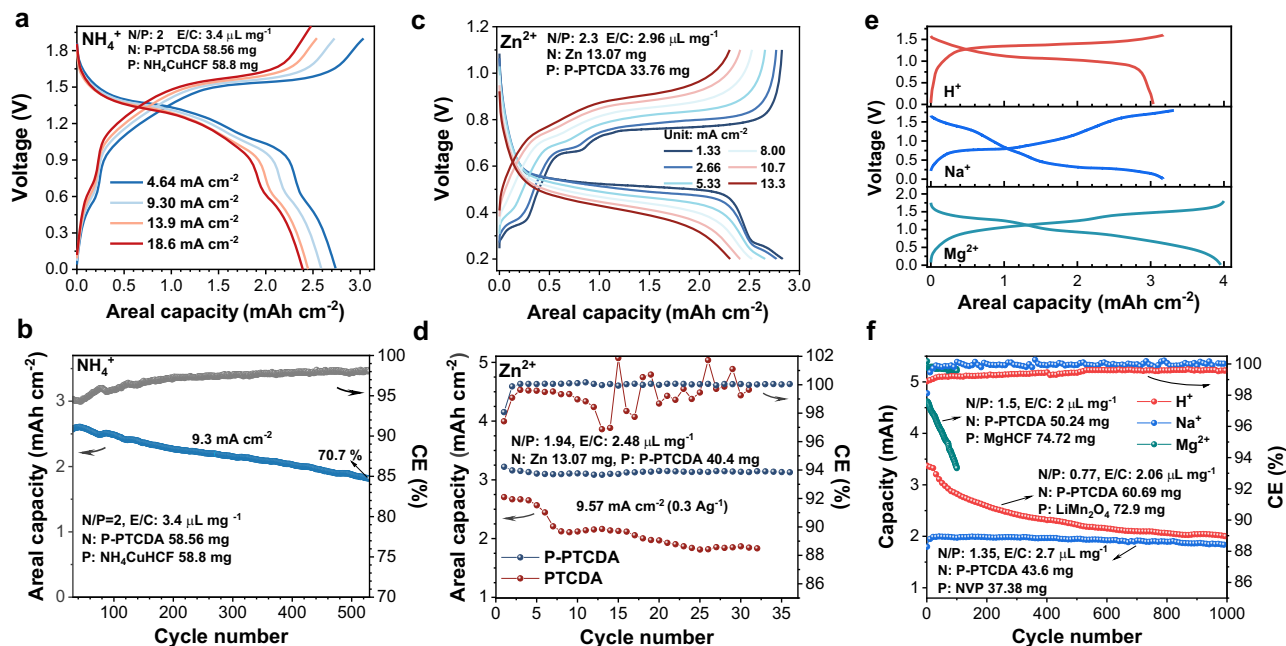


Fig. 5 | POEs for various battery systems under 3H3L condition. NH_4^+ ion batteries: **a** GCD profiles, **b** cycling performance of POEs for aqueous ammonium ion batteries. Zn^{2+} ion batteries: **c** GCD profiles, and **d** cycling performance of

PTCDA and P-PTCDA electrodes for aqueous zinc ion batteries. **e**, **f** H^+ , Na^+ , and Mg^{2+} ion batteries. **e** GCD profiles and **f** cycling performance. Source data are provided as a Source Data file.

Supplementary Fig. S2). Furthermore, P-ZnSN cells significantly extend the lifespan from 9 cycles to 75 cycles and increase the accumulated capacity from 18.7 mAh to 151.5 mAh compared to ZnSN cells, all while maintaining a discharge plateau of 1.1 V (Fig. 6j, m and Supplementary Fig. S3–S5)⁵⁰. These results validate the enhanced reversibility, rate, and cycling performance enabled by POEs. Above findings underscore analogous structural, property, and performance changes across diverse organic materials (molecule, polymer, and salt) akin to those observed in PTCDA post-pressure treatment, implying the broad applicability of the proposed POE technology towards practical organic batteries.

Discussion

In summary, we have developed pressurized organic electrode (POE) technology, offering a simple yet powerful approach for practical organic batteries with “3H3L” characteristics. High pressure induces significant structural and property changes in PTCDA material and electrode, including shape alteration, enhanced π - π interaction, narrowed band gap, oriented crystal planes, crystal size reduction, and surface vacancy formation. These alterations lead to increased density, favorable porosity/tortuosity, improved chemical reactivity, enhanced electronic conductivity, thermal stability, and mechanical strength in P-PTCDA electrodes. As a consequence, P-PTCDA electrodes treated at higher pressures exhibit larger capacities, faster charging/discharging rates, and longer cycle life in practical battery systems compared to their counterparts with no or lower pressure treatment. Notably, POE technology allows for aqueous batteries to operate under extreme conditions, including high mass loadings of up to 150 mg cm^{-2} and high AM fraction up to 95%, achieved under low N/P ratio and lean electrolyte conditions, resulting in a high energy density of 112.6 Wh L^{-1} . Encouragingly, POE technology demonstrates broad applicability across various battery systems (including Li^+ , Na^+ , H^+ , NH_4^+ , Zn^{2+} , and Mg^{2+} ion batteries) and organic materials (such as molecule, polymer, and salt), effectively overcoming previous limitations of unsuitable organic electrodes. Ongoing research in our lab focuses on exploring the applicability of POEs in other organic compounds and non-aqueous batteries, as well as investigating their potential for recycling

and upcycling. Overall, pressure emerges as a promising enabling tool, paving the way for the commercialization of practical and extreme organic batteries. This development heralds a transformative era in sustainable energy storage, offering exciting prospects for advancing the field of sustainable energy storage.

Methods

Chemicals

Perylene 3, 4, 9, 10-tetracarboxylic dianhydride (PTCDA, 98%), 1, 4, 5, 8-naphthalenetetracarboxylic dianhydride (NTCDA, 97%), ethylene diamine (EDA, 99%), lithium triflate (LiOTf , 98%), magnesium triflate ($\text{Mg}(\text{OTf})_2$, 98%) were purchased from TCI America. Lithium hydroxide (LiOH , 98%), ammonium hydroxide solution (28–30 wt%), N, N-dimethylformamide (DMF, 99.8%), N,N-dimethylacetamide (DMA, 99%), 1-methyl-2-pyrrolidone (NMP, 99%), sulfuric acid (H_2SO_4 , 95–98%), ammonium sulfate ($(\text{NH}_4)_2\text{SO}_4$, 99%), zinc sulfate heptahydrate ($\text{ZnSO}_4 \cdot 7\text{H}_2\text{O}$, 98%), copper sulfate pentahydrate ($\text{CuSO}_4 \cdot 5\text{H}_2\text{O}$, 99%), and Zn foil (250 μm , 99%) were obtained from Thermo Fisher Scientific. Sodium nitrate (NaNO_3 , 99%), magnesium sulfate heptahydrate ($\text{MgSO}_4 \cdot 7\text{H}_2\text{O}$, 99%), potassium hexacyanoferrate (II) trihydrate ($[\text{K}_4\text{Fe}(\text{CN})_6] \cdot 3\text{H}_2\text{O}$, 98.5%) was purchased from Sigma-Aldrich. Electrode materials including LiMn_2O_4 (LMO), $\text{Na}_3\text{V}_2(\text{PO}_4)_3$ (NVP), and Zn foil (10 μm , 99.99%) were purchased from Canrud (China). Industrial multiwalled CNT (MWCNT, carbon purity 90%) was supplied from Nanocyl.

Synthesis of P-PTCDA

PTCDA powder (1g) was poured into a die mold with a diameter of 12.7 mm and pressed under high pressure (e.g., 10 tons) for 10–30 s, resulting in a free-standing pellet. The pellet was crushed into P-PTCDA powder using mortar and pestle.

Synthesis of PTCDI nanofiber

100 mg of PTCDA and 10 mL of ammonia solution (25–30 wt.%) were added into a Teflon-lined autoclave (80 mL) followed by hydrothermal reaction at 80 $^\circ\text{C}$ for 12 h. PTCDI nanofibers were obtained after drying in fume hood (to remove ammonia) and freeze-drying (to remove water, -40 $^\circ\text{C}$ for 24 h).

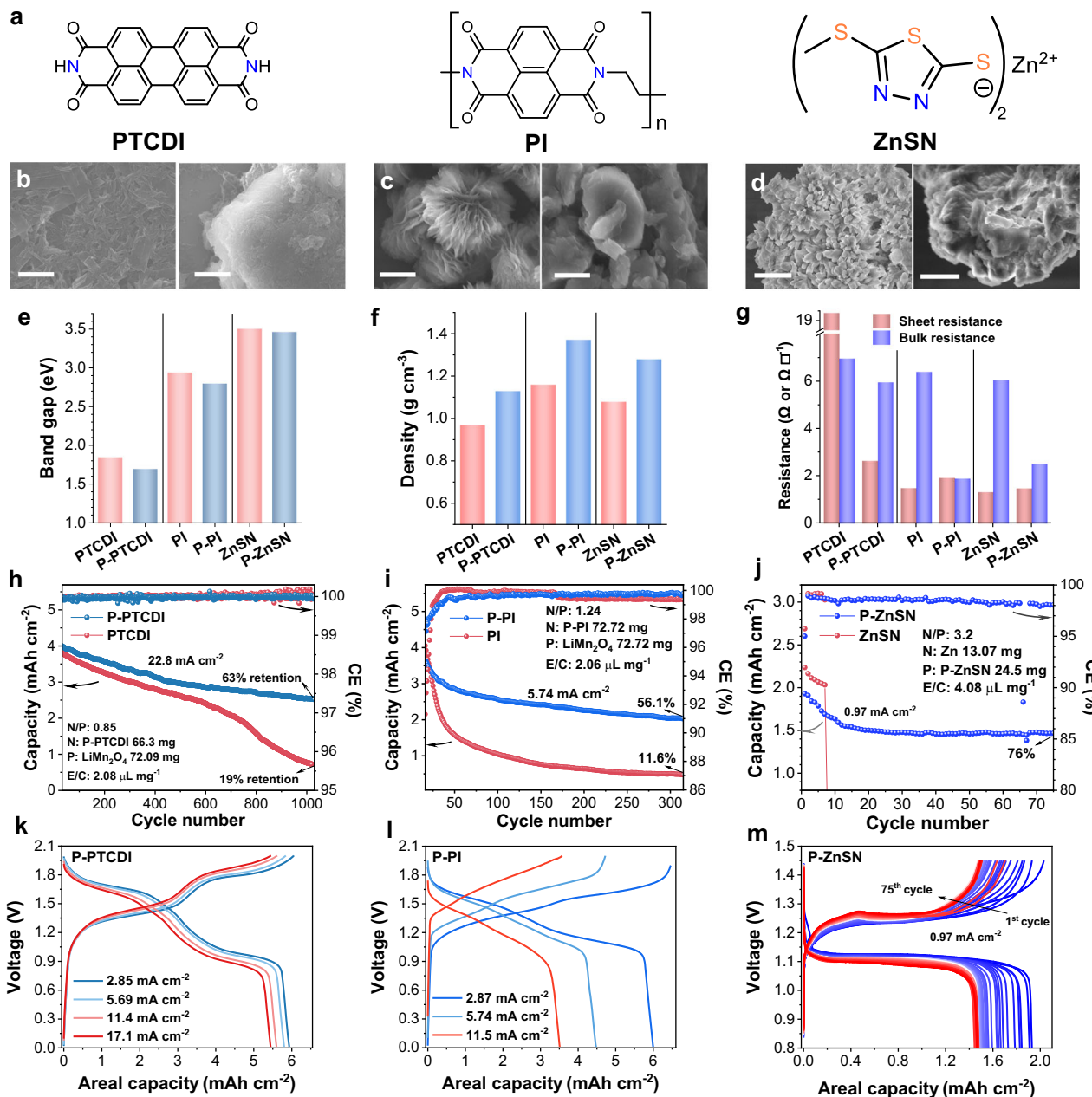


Fig. 6 | POEs for various organic materials and batteries. a Molecular structure of PTCDI, PI, and ZnSN. **b–d** SEM images of PTCDI, P-PTCDI, PI, P-PI, ZnSN, and P-ZnSN (left: pristine sample, right: pressurized sample). Scale bars, **b** 1 μm , **c** 500 nm, **d** 2 μm . **e** Optical band gap of PTCDI, PI, and ZnSN before and after pressure treatment.

f Density and **g** resistance of PTCDI, P-PTCDI, PI, P-PI, ZnSN, and P-ZnSN derived electrodes. Cycling performance of **h** PTCDI and P-PTCDI, **i** PI and P-PI, and **j** ZnSN and P-ZnSN cells. Charge-discharge profiles of POE-based cells at different rates or cycles: **k** P-PTCDI, **l** P-PI, **m** P-ZnSN. Source data are provided as a Source Data file.

Synthesis of PI microflower

NTCDA and EDA (molar ratio: 1.01:1) was successively added into a round-shaped flask containing 60 mL NMP and the pre-polymerization reaction was conducted at room temperature for 1 h⁵¹. Then the mixture was poured into a Teflon-lined autoclave (80 mL) for solvothermal polymerization at 190 °C for 6 h. PI microflower was obtained after vacuum filtration, washing (using DMF, water, and ethanol for three times), and drying at 80 °C overnight.

Synthesis of NH_4CuHCF and MgHCF

40 mL 0.1 M $\text{CuSO}_4 \cdot 5\text{H}_2\text{O}$ (998.7 mg) solution was dropped in 30 min into 40 mL 0.1 M $\text{K}_4\text{Fe}(\text{CN})_6$ (1.689 g) solution under stirring⁴⁵. After reaction for 6 h, precipitate was collected after centrifugal washing and oven drying, giving rise to $\text{Na}_2\text{Cu}[\text{Fe}(\text{CN})_6]$. This product (0.5 g)

was further dispersed in 40 mL 1 M $(\text{NH}_4)_2\text{SO}_4$ or MgSO_4 for ion exchange reaction under stirring for 6 h. After washing and drying, the NH_4CuHCF or MgHCF was obtained.

Making of free-standing organic electrodes

PTCDA or P-PTCDA powder (default: 80 wt.%) was hand mixed with MWCNT powder (default: 20 wt.%) in the mortar for 10–20 min. The powder mixture was poured into the die mold and pressed under high pressure (3 tons for 3T-PTCDA, 6 tons for 6T-PTCDA, and 10 tons for 10T-PTCDA and 10T-PTCDA) for 20 s to obtain free-standing and binder-free POEs. Cold pressing was performed at room temperature (22 ± 2 °C) under ambient atmospheric conditions. Typical mass loading of POEs is around 50 mg cm^{-2} with a diameter of 1.27 cm. POEs with high mass loadings of

100–150 mg cm⁻² and high AM fraction (90% and 95%) have also been prepared.

Making of free-standing counter electrodes

To pair with organic electrodes, free-standing counter electrodes were prepared including LMO/CNT, NVP/CNT, NH₄CuHCF/CNT, and MgHCF/CNT in a similar way to organic electrodes (mix and press), except that the AM fraction is different, 90% for LMO/CNT, 70% for NVP/CNT, and 80% for NH₄CuHCF/CNT or MgHCF/CNT electrodes. To achieve low N/P ratios (0.8–3, based on theoretical capacity), the mass loading of counter electrodes is adjusted according to the loading of organic electrodes, typically in the range of 30–150 mg cm⁻². While theoretical capacity of PTCDA (2e transfer) and LMO is 136.6 and 148 mAh g⁻¹, respectively, the achievable capacity for LMO is around 120–130 mAh g⁻¹. So a low N/P ratio of 0.8 is reasonable in our PTCDA||LMO cells.

Making of other organic electrodes

Powders of PTCDI, PI, and ZnSN were pressed and crushed to make corresponding P-PTCDI, P-PI, P-ZnSN, respectively. Then PTCDI, P-PTCDI, PI, P-PI, ZnSN, and P-ZnSN powders were mixed with CNT and compressed into free-standing electrodes. AM fraction is 80% for PTCDI, P-PTCDI, PI, P-PI and 70% for ZnSN, P-ZnSN.

Characterization

All samples were prepared in the open atmosphere at room temperature (22 ± 2 °C). The chemical structure of organic materials was studied by Fourier Transform Infrared Spectroscopy (FTIR, Nicolet iS50) in an ATR mode with powders pressed onto a diamond window. X-ray Diffraction (XRD) measurements were conducted on an Ultima IV (Rigaku) diffractometer equipped with a Cu K α X-ray source. The 2D-WAXD patterns of powder and pellet samples were measured with the Rigaku Rapid II X-rays at a voltage of 45 kV and a current of 66 mA. The wavelength of the X-ray beam source equipped with an ultra-high-intensity microfocus rotating anode of copper is 0.154 nm. The X-ray measurement geometry with the incident beam perpendicular to the top and side of pellet sample is shown in the inset of Fig. 1h. UV-visible spectra were recorded using a Perkin-Elmer NIR-UV Spectrophotometer, where sample powder was coated on a thin glass plate with double-sided tape (both glass plate and tape show negligible absorbance in the test range). Material micro/nano-structures were characterized by field-emission scanning electron microscope (FESEM, Zeiss Sigma) equipped with energy dispersive X-ray analysis (EDX, Oxford) and sphere-aberrated transmission electron microscope (TEM, JEOL JEM-ARM200CF) equipped with Atomic Resolution S/TEM. For SEM test, powdery samples were dispersed in ethanol and dropped onto a silicon wafer and attached onto an Al stub while pellet samples were directly mounted on the stub before testing. For TEM test, powders were dispersed in ethanol and dropped onto a Cu grid. The surface roughness of electrodes was measured by an Olympus Laser Confocal Scanning Microscope (LCSM, OLS3000). X-ray photoelectron spectrometer (XPS, Kratos AXIS Ultra) was used to gain insight into the chemical binding environment of elements.

Electron paramagnetic resonance (EPR) spectra were collected using Bruker ELEXSYS EPR spectrometer operated at 0.0001 T modulation amplitude, 100,000 Hz modulation frequency, 9.865601 GHz microwave frequency and 0.02 W microwave power with signals centered at 3505 Gauss and scanned for 10 times. Powdery samples were filled into a quartz tube for the EPR test.

Synchrotron X-ray computed tomography was carried out at the Biomedical Imaging and Therapy Facility (BMIT) 05B1-1 beamline at the Canadian Light Source. A white beam filtered by an Ag attenuator was used, creating a spectrum with an effective mean X-ray energy of around 24 keV. Three-dimensional datasets were acquired using a PCO Edge 5.5 camera (PCO, Germany) equipped with a 20- μ m-thick LuAG

scintillator and a 5 \times optical system (Optique Peter, Lentilly, France), yielding cubic voxels of 1.44 μ m. Imaging was conducted at ~20% of the camera's dynamic range, with 2500 projections collected over a sample-to-detector distance of 50 cm. Phase retrieval, ring artefact suppression, and tomographic reconstruction were performed using the tofu software package.

The thermal property was characterized by Thermogravimetric Analyzer (TGA Q50) in the air atmosphere with a heating rate of 10 °C/min. Sheet resistance of organic electrodes was measured by the four-point probe (Pro4 4000) and data was collected by averaging 3–5 test points. Bulk resistance of POEs was tested by sandwiching the POE (100–150 mg) with two pieces of stainless steel plates (1.5 mm thickness) and the voltage-current curves were measured by workstation (biologic, VMP3) in a linear scanning voltammogram technique. Mechanical compression test was conducted on a universal test machine (Instron 5966 Dual Column Table Frame, 100 kN load cell with a background noise of approximately ± 1 N), where samples (4 mm diameter and ~1.5 mm thickness, prepared in a 4 mm mold under a force of 1 ton) were subjected to compression between two flat plates. Chemical kinetics were studied by pouring 2 M LiOH solution into PTCDA or P-PTCDA powder and reaction changes were recorded by a digital camera.

Electrochemical measurements

Battery performance was evaluated based on coin cells (CR2032 or CR2016). Free-standing organic electrodes and counter electrodes (LMO/CNT, NVP/CNT, NH₄CuHCF/CNT, MgHCF/CNT, and Zn foil) were sandwiched by a glassy fiber separator (Whatman GF A, thickness: 0.26 mm, diameter: 18 mm, average pore size: 1.6 μ m). For ZnSN and P-ZnSN electrodes, an ion exchange membrane was used as the separator⁵⁰. Aqueous electrolyte were prepared for different systems including 4 M LiOTf for lithium-ion battery, 5 M NaNO₃ for sodium-ion battery, 2 M H₂SO₄ for proton battery, 4 M (NH₄)₂SO₄ for ammonium-ion battery, 2.5 M Mg(OTf)₂ for magnesium-ion battery, and 2 M ZnSO₄ for zinc-ion battery. Hybrid electrolyte based on 10% (v) of DMA (2 M ZnSO₄-10%DMA) was also adopted for zinc ion batteries to suppress the severe dendrite growth of zinc metal under high rates and high areal capacities⁵². Lean electrolyte ranging from 100 to 400 μ L is controlled to achieve a E/C value of 1.5–3 μ L mg⁻¹ according to the mass of positive electrode materials. Cells were assembled by the crimper at a pressure of ~5 MPa (5 s) and rested for 1–5 h before cycling. Cells were tested at 22 ± 2 °C without a climatic/environmental chamber.

In situ EIS measurements were performed on PTCDA||LMO and P-PTCDA||LMO cells using an electrochemical workstation (Biologic VMP300) with the galvanostatic signal (GEIS). The frequency range for the EIS was set from 300 kHz to 50 mHz with 6 points per decade of frequency collected. The testing protocol involved galvanostatically charging the cells for 20 min followed by a rest period of 20 minutes or discharging for 20 min followed by a 20 min rest period, and then EIS test for ~6 min 20 s at the quasi-stationary potential, for the first and second cycle. For the 101st cycle, the charge/discharge duration was extended to 40 min. The current density for in situ EIS cycles was maintained at 0.05 A g⁻¹, while long-term cycling (3rd–100th cycle) was conducted at a higher rate of 0.3 A g⁻¹ on the battery cyclers.

Computational calculation

Theoretical models and XRD data were constructed by Gaussian 16 and Materials Studio 2023.

Calculation of specific/areal/volumetric energy and power densities.

The specific energy *E* (Wh kg⁻¹) and specific power *P* (W kg⁻¹) of batteries were calculated based on the following equations:

$$E = \frac{1000 \cdot \int IV(t)dt}{m} \quad (1)$$

$$P = \frac{E}{t} \quad (2)$$

in which $V(t)$, I , dt , and m represents discharge voltage (V), current (A), discharge time (h), the mass (g) of active materials in the positive electrode, respectively.

The areal energy density E (Wh cm⁻²) and power density P (W cm⁻²) were calculated based on the following equations:

$$E = \frac{1000 \cdot \int IV(t)dt}{A} \quad (3)$$

$$P = \frac{E}{t} \quad (4)$$

in which $V(t)$, I , dt , and A represents discharge voltage (V), current (A), differential time (h), and the area (cm²) of active materials in the positive electrode, respectively. $A = 1.267$ cm² in our electrodes.

Data availability

The data supporting the findings of the study are included in the main text and supplementary information files. Additional data can be obtained from the corresponding author upon request. Source data are provided with this paper.

References

- Kim, J. et al. Organic batteries for a greener rechargeable world. *Nat. Rev. Mater.* **8**, 54–70 (2023).
- Nguyen, T. P. et al. Polypeptide organic radical batteries. *Nature* **593**, 61–66 (2021).
- Liang, Y. et al. Universal quinone electrodes for long cycle life aqueous rechargeable batteries. *Nat. Mater.* **16**, 841–848 (2017).
- Armand, M. et al. Conjugated dicarboxylate anodes for Li-ion batteries. *Nat. Mater.* **8**, 120–125 (2009).
- Wang, J. et al. Conjugated sulfonamides as a class of organic lithium-ion positive electrodes. *Nat. Mater.* **20**, 665–673 (2021).
- Grignon, E., Battaglia, A. M., Schon, T. B. & Seferos, D. S. Aqueous zinc batteries: design principles toward organic cathodes for grid applications. *iScience* **25**, 104204 (2022).
- Muench, S. et al. Polymer-based organic batteries. *Chem. Rev.* **116**, 9438–9484 (2016).
- Lu, Y., Zhang, Q., Li, L., Niu, Z. & Chen, J. Design strategies toward enhancing the performance of organic electrode materials in metal-ion batteries. *Chem* **4**, 2786–2813 (2018).
- Li, M. et al. Electrolytes in organic batteries. *Chem. Rev.* **123**, 1712–1773 (2023).
- Zhao, Q. et al. High-capacity aqueous zinc batteries using sustainable quinone electrodes. *Sci. Adv.* **4**, eaao1761 (2018).
- Wang, F. et al. High-voltage aqueous magnesium ion batteries. *ACS Cent. Sci.* **3**, 1121–1128 (2017).
- Suo, L. et al. Water-in-saltTM electrolyte enables high-voltage aqueous lithium-ion chemistries. *Science* **350**, 938–943 (2015).
- Molina, A. et al. Electrode engineering of redox-active conjugated microporous polymers for ultra-high areal capacity organic batteries. *ACS Energy Lett.* **5**, 2945–2953 (2020).
- Lee, M. et al. High-performance sodium–organic battery by realizing four-sodium storage in disodium rhodizonate. *Nat. Energy* **2**, 861–868 (2017).
- Lu, Y. & Chen, J. Prospects of organic electrode materials for practical lithium batteries. *Nat. Rev. Chem.* **4**, 127–142 (2020).
- Bitenc, J., Pirnat, K., Lužanin, O. & Dominko, R. Organic cathodes, a path toward future sustainable batteries: mirage or realistic future? *Chem. Mater.* **36**, 1025 (2024).
- lordache, A. et al. From an enhanced understanding to commercially viable electrodes: the case of PTCLi4 as sustainable organic lithium-ion anode material. *Adv. Sustain. Syst.* **1**, 1600032 (2017).
- Fan, L., Ma, R., Wang, J., Yang, H. & Lu, B. An ultrafast and highly stable potassium–organic battery. *Adv. Mater.* **30**, 1805486 (2018).
- Xu, Z. et al. An ultrafast, durable, and high-loading polymer anode for aqueous zinc-ion batteries and supercapacitors. *Adv. Mater.* **34**, 2200077 (2022).
- Hatakeyama-Sato, K., Wakamatsu, H., Katagiri, R., Oyaizu, K. & Nishide, H. An ultrahigh output rechargeable electrode of a hydrophilic radical polymer/nanocarbon hybrid with an exceptionally large current density beyond 1 A cm⁻². *Adv. Mater.* **30**, 1800900 (2018).
- Chen, T. et al. A layered organic cathode for high-energy, fast-charging, and long-lasting Li-ion batteries. *ACS Cent. Sci.* **10**, 569 (2024).
- Han, C., Li, H., Li, Y., Zhu, J. & Zhi, C. Proton-assisted calcium-ion storage in aromatic organic molecular crystal with coplanar stacked structure. *Nat. Commun.* **12**, 2400 (2021).
- Guo, Z. et al. An organic/inorganic electrode-based hydronium-ion battery. *Nat. Commun.* **11**, 959 (2020).
- Chen, Y. et al. A recyclable and scalable high-capacity organic battery. *Angew. Chem. Int. Ed.* **62**, e202302539 (2023).
- Sun, H. et al. Signatures of superconductivity near 80 K in a nickelate under high pressure. *Nature* **621**, 493–498 (2023).
- Kong, P. et al. Superconductivity up to 243 K in the yttrium-hydrogen system under high pressure. *Nat. Commun.* **12**, 5075 (2021).
- Deng, L. et al. Pressure-induced high-temperature superconductivity retained without pressure in FeSe single crystals. *Proc. Natl. Acad. Sci. USA* **118**, e2108938118 (2021).
- Wang, Y. et al. Giant pressure-driven lattice collapse coupled with intermetallic bonding and spin-state transition in manganese chalcogenides. *Angew. Chem. Int. Ed.* **55**, 10350–10353 (2016).
- Xiao, G. et al. Pressure effects on structure and optical properties in cesium lead bromide Perovskite Nanocrystals. *J. Am. Chem. Soc.* **139**, 10087–10094 (2017).
- Fang, C. et al. Pressure-tailored lithium deposition and dissolution in lithium metal batteries. *Nat. Energy* **6**, 987–994 (2021).
- Ghimire, P. C. et al. A comprehensive study of electrode compression effects in all vanadium redox flow batteries including locally resolved measurements. *Appl. Energy* **230**, 974–982 (2018).
- Famprakis, T. et al. Under pressure: mechanochemical effects on structure and ion conduction in the sodium-ion solid electrolyte Na3PS4. *J. Am. Chem. Soc.* **142**, 18422–18436 (2020).
- Driscoll, L. L. et al. Under pressure: offering fundamental insight into structural changes on ball milling battery materials. *Energy Environ. Sci.* **16**, 5196–5209 (2023).
- Fang, J. et al. Piezochromism in dynamic three-dimensional covalent organic frameworks. *Angew. Chem. Int. Ed.* **62**, e202304234 (2023).
- Zhang, H., Fang, Y., Yang, F., Liu, X. & Lu, X. Aromatic organic molecular crystal with enhanced π – π stacking interaction for ultrafast Zn-ion storage. *Energy Environ. Sci.* **13**, 2515–2523 (2020).
- Diao, J. et al. Research progress on binders for silicon-based anodes. *J. Power Sour.* **625**, 235665 (2025).
- Liu, N. et al. A pomegranate-inspired nanoscale design for large-volume-change lithium battery anodes. *Nat. Nanotechnol.* **9**, 187–192 (2014).
- Zhao, K., Pharr, M., Vlassak, J. & Suo, Z. Fracture of electrodes in lithium-ion batteries caused by fast charging. *J. Appl. Phys.* **108**, 073517 (2010).
- Wan, T. H., Saccoccio, M., Chen, C. & Ciucci, F. Influence of the discretization methods on the distribution of relaxation times

- deconvolution: implementing radial basis functions with DRTtools. *Electrochim. Acta* **184**, 483 (2015).
40. Kim, D. J. et al. Rechargeable aluminium organic batteries. *Nat. Energy* **4**, 51–59 (2019).
 41. Jiang, L. et al. Building aqueous K-ion batteries for energy storage. *Nat. Energy* **4**, 495–503 (2019).
 42. Lin, Z. et al. A high capacity small molecule quinone cathode for rechargeable aqueous zinc-organic batteries. *Nat. Commun.* **12**, 4424 (2021).
 43. Li, W. et al. Tuning electron delocalization of hydrogen-bonded organic framework cathode for high-performance zinc-organic batteries. *Nat. Commun.* **14**, 5235 (2023).
 44. Xie, J., Liang, Z. & Lu, Y.-C. Molecular crowding electrolytes for high-voltage aqueous batteries. *Nat. Mater.* **19**, 1006–1011 (2020).
 45. Park, S.-H. et al. High areal capacity battery electrodes enabled by segregated nanotube networks. *Nat. Energy* **4**, 560–567 (2019).
 46. Luo, J.-Y., Cui, W.-J., He, P. & Xia, Y.-Y. Raising the cycling stability of aqueous lithium-ion batteries by eliminating oxygen in the electrolyte. *Nat. Chem.* **2**, 760–765 (2010).
 47. Lee, J. T., Jo, C. & De Volder, M. Bicontinuous phase separation of lithium-ion battery electrodes for ultrahigh areal loading. *Proc. Natl. Acad. Sci. USA* **117**, 21155–21161 (2020).
 48. Wu, J. et al. Low-tortuosity thick electrodes with active materials gradient design for enhanced energy storage. *ACS Nano* **16**, 4805–4812 (2022).
 49. Wu, X. et al. Rocking-chair ammonium-ion battery: a highly reversible aqueous energy storage system. *Angew. Chem. Int. Ed.* **56**, 13026–13030 (2017).
 50. Tuttle, M. R. et al. Redox-active zinc thiolates for low-cost aqueous rechargeable Zn-ion batteries. *Chem. Sci.* **12**, 15253–15262 (2021).
 51. Xu, Z. et al. Nitrogen-doped porous carbon superstructures derived from hierarchical assembly of polyimide nanosheets. *Adv. Mater.* **28**, 1981–1987 (2016).
 52. Deng, W., Xu, Z. & Wang, X. High-donor electrolyte additive enabling stable aqueous zinc-ion batteries. *Energy Storage Mater* **52**, 52–60 (2022).

Acknowledgements

This work was financially supported by the Natural Sciences and Engineering Research Council of Canada (NSERC), through the Discovery Grant Program (RGPIN-2018-06725, X.W.) and the Discovery Accelerator Supplement Grant program (RGPAS-2018-522651, X.W.), and by the New Frontiers in Research Fund-Exploration program (NFRFE-2019-00488, X.W.). Prof. Xiaolei Wang acknowledges the support from Canada Research Chair Program (CRC-2022-00059, X.W.), and the Canada First Research Excellence Fund as part of the University of Alberta's Future Energy Systems research initiative (FES-T06-Q03, X.W.). Dr. Zhixiao Xu received support from the CLSI Student Travel Support Program. The μ CT was performed at the beamline BM1-BM at the Canadian Light Source, a national research facility of the University of Saskatchewan, which is supported by the Canada Foundation for Innovation (CFI), NSERC, the National Research Council (NRC), the Canadian Institutes of

Health Research (CIHR), the Government of Saskatchewan, and the University of Saskatchewan. The organic material (ZnSN) provided by Prof. Shiyu Zhang at the Ohio State University is also appreciated.

Author contributions

X.W., J.L., G.L., and Z. X. conceived the idea and designed the experiments. X.W., J.L., and G. L. supervised the research. Z.X. prepared materials, conducted electrochemical measurements and structural characterizations. Y.X. helped with analysis. Y.C. and Y.Q. conducted 2D WAXD characterizations and structural simulations. S.G. helped with synchrotron-based X-ray computed tomography test. All authors discussed the results and contributed to manuscript preparation.

Competing interests

The authors declare no competing interests.

Additional information

Supplementary information The online version contains supplementary material available at <https://doi.org/10.1038/s41467-025-59892-y>.

Correspondence and requests for materials should be addressed to Ge Li, Jun Lu or Xiaolei Wang.

Peer review information *Nature Communications* thanks Nicholas Siemons, and the other, anonymous, reviewer(s) for their contribution to the peer review of this work. A peer review file is available.

Reprints and permissions information is available at <http://www.nature.com/reprints>

Publisher's note Springer Nature remains neutral with regard to jurisdictional claims in published maps and institutional affiliations.

Open Access This article is licensed under a Creative Commons Attribution-NonCommercial-NoDerivatives 4.0 International License, which permits any non-commercial use, sharing, distribution and reproduction in any medium or format, as long as you give appropriate credit to the original author(s) and the source, provide a link to the Creative Commons licence, and indicate if you modified the licensed material. You do not have permission under this licence to share adapted material derived from this article or parts of it. The images or other third party material in this article are included in the article's Creative Commons licence, unless indicated otherwise in a credit line to the material. If material is not included in the article's Creative Commons licence and your intended use is not permitted by statutory regulation or exceeds the permitted use, you will need to obtain permission directly from the copyright holder. To view a copy of this licence, visit <http://creativecommons.org/licenses/by-nc-nd/4.0/>.

© The Author(s) 2025